

27. K. Efimenko, J. Genzer, in preparation.
 28. N. Bowden, S. Brittain, A. G. Evans, J. W. Hutchinson, G. M. Whitesides, *Nature* **393**, 146 (1998).
 29. The PDMS networks are prepared from the commercial PDMS Sylgard 184 and the curing agent 184 (Dow Corning). The PDMS:curing agent ratio is 10:1, as recommended by the recipe provided by the manufacturer.
 30. Previously, oxygen plasma was used to produce thin layers of SiO_x on the PDMS surfaces (24). We chose UVO rather than an oxygen plasma because the UVO treatment, at the wavelength of $\lambda = 254$ nm, does not cover the surface of PDMS with a continuous SiO_x layer (25, 26), as confirmed from combined experiments with a palette of experimental probes that included Fourier transform infrared spectrometry in the attenuated total reflection, NEXAFS, x-ray reflectivity, and contact angle measurements (27).

- Hence, the mechanical properties of the PDMS substrates are not altered as much as in the case of oxygen plasma-treated PDMS (9, 28).
 31. The SAM deposition experiments are usually done in a desiccator that is connected to a mechanical vacuum pump. The vacuum level in the deposition chamber is $\approx 10^{-2}$ to 10^{-3} torr, so that there is still a sufficient amount of water molecules needed for reaction 1. The sample is placed upside down above the diffusion source, which consists of a mixture of the chlorosilane and paraffin oil. Because the paraffin oil does not mix with the chlorosilane molecules, it provides a convenient dilutant medium for the diffusion source; the flux of the FyHx molecules can be conveniently adjusted by simply varying the FyHx:paraffin oil ratio.
 32. Contact angle experiments were performed with a Ramé-Hart contact angle goniometer, model 100-00.

- The advancing contact angles were read by injecting 4 μ l of deionized water; the receding contact angles were determined by removing 3 μ l of deionized water from the droplet. Each data point reported here represents an average over four measurements on the same sample.
 33. Supported by the North Carolina State University College of Engineering startup funds and the NSF CAREER award, grant DMR98-75256. NEXAFS experiments were carried out at the National Synchrotron Light Source, Brookhaven National Laboratory, which is supported by the U.S. Department of Energy, Division of Materials Sciences and Division of Chemical Sciences. We thank D. A. Fischer and W. E. Wallace for their assistance during the course of the NEXAFS experiments.

7 August 2000; accepted 8 November 2000

External Control of 20th Century Temperature by Natural and Anthropogenic Forcings

Peter A. Stott,^{1*} S. F. B. Tett,¹ G. S. Jones,¹ M. R. Allen,² J. F. B. Mitchell,¹ G. J. Jenkins¹

A comparison of observations with simulations of a coupled ocean-atmosphere general circulation model shows that both natural and anthropogenic factors have contributed significantly to 20th century temperature changes. The model successfully simulates global mean and large-scale land temperature variations, indicating that the climate response on these scales is strongly influenced by external factors. More than 80% of observed multidecadal-scale global mean temperature variations and more than 60% of 10- to 50-year land temperature variations are due to changes in external forcings. Anthropogenic global warming under a standard emissions scenario is predicted to continue at a rate similar to that observed in recent decades.

Over the last three decades, global mean temperature near Earth's surface has been increasing at a rate of 0.2 K/decade. This rise is unusually rapid compared to model estimates of natural internal variability (1–3). It is also unusual in the context of reconstructions of the past 1000 years from paleodata (4, 5). Simplified energy balance models of the climate system have been used to simulate global mean climate (6, 7), but they are not able to represent spatial patterns of temperature change, and their sensitivity must be tuned to fit the observations. Three-dimensional climate models are capable of producing good agreement with the observed warming of the last three decades if they include both greenhouse gases and the cooling effects of sulfate aerosols (1, 8–10).

A rise in near-surface temperatures as rapid as that during the last 30 years occurred over several decades during the first half of the 20th century, followed by a period of more than three decades when temperatures showed no long-term increase. The net radiative forcing of the atmosphere from the combined effects of greenhouse gases and sulfate aerosols is estimated to have increased more rapidly after 1960 than before (8). Consequently, climate models that include these two forcing factors alone have not generally been as successful at simulating climate change during the early part of the century. During this period, there were few explosive volcanic eruptions (11) and total solar irradiance was generally increasing from one solar cycle to the next (12), suggesting a possible natural origin of this warming trend. Various “detection and attribution” studies suggested that natural forcings may have contributed significantly to this early-century warming (3, 9, 10, 13), but the warming has also been attributed to an unusually large instance of internal variability (2, 14).

Here, we made an ensemble of simulations using a coupled ocean-atmosphere general circulation model that includes both the most important anthropogenic forcings and the most important natural forcings (15) during the 20th century. The model we use is HadCM3 (16, 17), a dynamical climate model which does not use flux adjustment (18). Our ensemble consists of four simulations that are identical except for their initial conditions. The initial conditions used were taken from states separated by 100 years in a 1300-year control run of HadCM3 in which external forcings have no year-to-year variations. The simulations in this ensemble incorporate changes in individual well-mixed greenhouse gases including carbon dioxide and methane (19), changes in tropospheric and stratospheric ozone, and changes in sulfur emissions. The direct effect of sulfate aerosols on planetary albedo is simulated using a fully interactive sulfur cycle scheme that models the emission, transport, oxidation, and removal of sulfur species. The indirect effect of tropospheric aerosol on cloud reflectivity (20) is also represented in the model. The simulations include natural forcings due to changes in the amount of stratospheric aerosols following explosive volcanic eruptions (21), and spectrally-resolved changes in solar irradiance (22). This ensemble is compared with two others; one of four simulations including the same anthropogenic forcings only and another of four simulations including the same natural forcings only. The three ensembles are named ALL, ANTHRO, and NATURAL, respectively.

The ALL ensemble captures the main features of global mean temperature changes observed since 1860 (Fig. 1, bottom). The approximately 0.2 K/decade rate of warming that is observed over the last three decades is reproduced by the model, and simulations and observations both show a similar rate of warming between 1910 and 1939. None of the NATURAL simulations shows a general warming over the last 30 years (Fig. 1, top), a period containing three major volcanic eruptions: Agung in 1963, El Chichón in 1982, and Mt. Pinatubo in 1991. In contrast, all four members of ANTHRO show warm-

¹Met Office, Hadley Centre for Climate Prediction and Research, Bracknell, Berkshire RG12 2SY, UK. ²Space Science and Technology Department, Rutherford Appleton Laboratory, Didcot, Oxfordshire OX11 0QX, UK and Department of Physics, University of Oxford, Oxford OX1 3PU, UK.

*To whom correspondence should be addressed. E-mail: pastott@meto.gov.uk

REPORTS

ing over the last three decades at a rate consistent with that observed (Fig. 1, middle). However, these latter simulations are consistently too cool during the 1940s and 1950s, unlike the simulations that include natural forcings (Fig. 1, top and bottom).

One of the ALL simulations has been extended to the year 2100, using estimates of future greenhouse gas and tropospheric ozone concentrations and sulfur emissions based on the B2 scenario of the Intergovernmental Panel on Climate Change (IPCC) Special Report on

Emissions Scenarios [SRES (23)]. This scenario is one of the marker scenarios that the IPCC has developed to provide more self-consistent and up-to-date scenarios for climate prediction than hitherto possible. Its assumptions about future demographic changes, economic development, and technological change result in more modest increases in greenhouse gases than the alternative A2 marker scenario (24). Stratospheric ozone is assumed to recover as atmospheric chlorine loading diminishes (25). Only the anthropogenic contribution to future climate change is forecast, since solar and volcanic forcings are assumed to remain at 1999 levels. The rate of change of global mean temperature predicted over the 21st century is similar to that already encountered (both in observations and in model simulations) since 1970, reaching 3 K by 2100 relative to 1880–1920 (Fig. 1).

When we include both anthropogenic and natural forcings, our model successfully simulates not just the observed global mean response, but also some of the large-scale features of the observed temperature response. Recent warming (26) has been greater over land (0.24 K/decade) than ocean (0.16 K/decade) (Fig. 2), and this is also seen in the model [ensemble mean trends of 0.25 ± 0.11 and 0.13 ± 0.06 K/decade over land and sea, respectively, with uncertainties calculated from the HadCM3 control run (27)]. The model captures much of the decadal smoothed evolution of land temperatures (Fig. 2A), including temperature fluctuations early in the century, but appears to underestimate the observed rate of increase of sea temperatures seen between 1910 and 1939 (Fig. 2B). Before 1940, data are sparse in the Pacific Ocean and in the Southern Hemisphere, but splitting Northern Hemisphere temperatures into land and sea components shows that the model underestimates the early-century increase in Northern Hemisphere Atlantic temperatures.

The roughly three-way split in the evolution of near-surface temperatures is captured by considering three 30-year trends starting in 1910, 1940, and 1970 (Fig. 3). In the first and last of these periods, global mean observed temperatures were increasing whereas in the second period, observed temperatures were gradually declining, and the simulations capture this approximately three-way division in the 20th-century history of Earth's near-surface temperatures. Global mean trends in ALL are consistent with observed trends in all three periods at the $P = 0.1$ (two-tailed) confidence level, i.e., differences between modeled and observed trends are within the 5 to 95% range expected from the control variability. For the 30-year trends from 1910 to 1939, the difference between the observed trend of 0.41 K per 30 years and the ensemble mean model trend is 0.28 K;

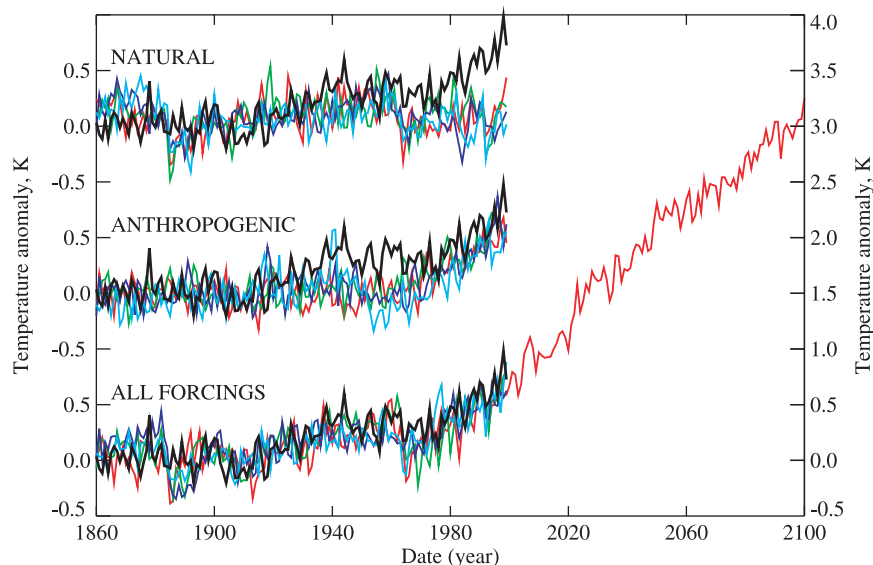


Fig. 1. Annual-mean global mean near-surface (1.5 m) temperature anomalies (relative to 1881–1920) for the NATURAL, ANTHRO, and ALL ensembles. Ensemble members are shown as colored lines, and observations [updated versions of surface temperature data set of Parker *et al.* (39)] are shown as a black line. All model data up to November 1999 are masked by the observational missing data mask and expressed, like the observations, as anomalies relative to 1961–1990. Future model data are masked by observational mask for year December 1998 to November 1999. Global means are then calculated and expressed as anomalies relative to 1881–1920.

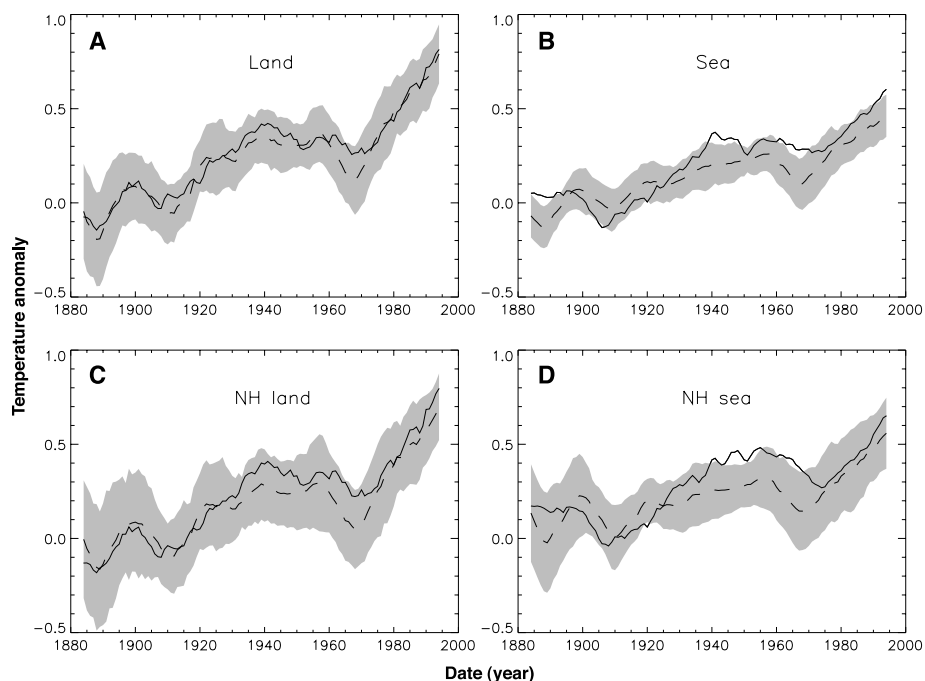


Fig. 2. Running decadal-mean global mean surface (1.5 m) temperature anomalies for (A) land, (B) ocean (sea), (C) Northern Hemisphere (NH) land, (D) Northern Hemisphere ocean (sea). Data are expressed as anomalies relative to the period 1961–1990 and masked as in Fig. 1. Solid black line, observations; dashed line, ALL ensemble mean. The gray shading shows the 5 and 95 percentiles of the expected uncertainty distribution of possible deviations from the model ensemble mean calculated from a long control simulation of HadCM3.

REPORTS

differences as large or larger than this occur $\sim 17\%$ of the time in the control integration. In contrast, the ANTHRO trend over this period is 0.06 K per 30 years, a discrepancy that occurs by chance $< 1\%$ of the time in the control. Likewise, the NATURAL trend over the 1970–1999 period is 0.03 K, compared to the observed trend of 0.57 K over 30 years, a discrepancy larger than any observed in the control. Thus, ALL is a significantly better fit to the observations over the 20th century than either ANTHRO or NATURAL alone.

Consideration of the spatial distributions of the three 30-year trends shows that the early-century warming was largest in the Atlantic and North America, whereas recent warming has been more widespread (Fig. 3). Although the model captures the broad features of the spatial patterns of temperature change, there are significant differences in the early-century trends that cannot be explained by internal variability in a large region of the tropical Atlantic [as measured by a local t test (28) at the $P = 0.10$ level], a

result consistent with other model simulations (14) and which may be related to climate models' coarse equatorial resolution of ocean dynamics (29).

Correlations between the mean of the ALL ensemble and the observed temperature time series over a range of time scales provide an indication of the role of external forcings in climate predictability. On subdecadal time scales, the global mean correlation is less than 0.11, indicating that the response to external forcing is dominated by internal variability. On 10- to 50-year time scales, the global mean (land) correlation is 0.63 (0.83), rising to 0.93 (0.89) if greater than 50-year variability is also included (30). External forcings are also important at continental scales, with correlations for North American land temperatures (170°W – 50°W , 10°N – 70°N) of 0.57 on 10- to 50-year time scales and 0.82 including all time scales greater than 10 years, and lower correlations for northwest European land temperatures (10°W – 50°E , 30°N – 70°N) of 0.47 on 10- to 50-year

time scales and 0.58 for greater than 10-year time scales. Both anthropogenic and natural factors contribute to the skill of the model (Fig. 1).

An upper bound on the potential skill of the model can be estimated by calculating the percentage of total variance explained by the model's response to external forcings (31). For global mean (land) temperatures this is 61% (63%) for 10- to 50-year time scales, rising to 89% (87%) if greater than 50-year variability is included, corresponding to correlations of 0.78 (0.79) and 0.94 (0.93), respectively. Consequently, large-scale temperature changes, particularly over land, may be predictable on multidecadal time scales if we know the boundary conditions provided by external forcings of the climate system, in contrast to predictability associated with accurate knowledge of atmospheric and oceanic initial conditions, which is unlikely to be useful on global scales beyond 2 years (32, 33). Given the uncertainties in historical forcing, climate sensitivity, and the rate of heat

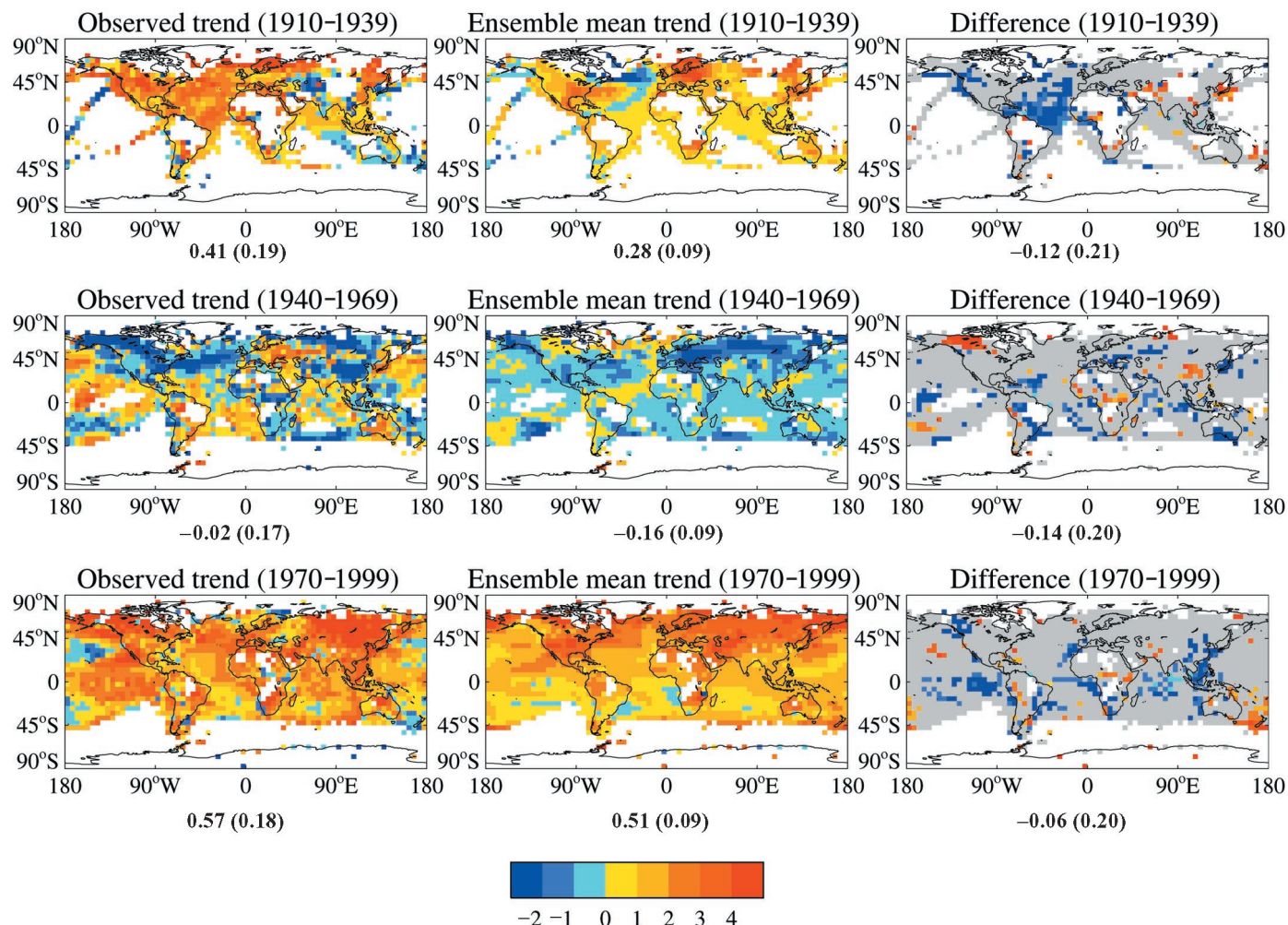


Fig. 3. Linear trends (K/30 years) of near-surface temperature for three 30-year periods spanning 1910 to 1999 from the observations, the ALL ensemble mean, and model-observational differences significant at the $P = 0.10$ level according to a two-sided t test. Gray shading denotes regions

where the observed and model trends are consistent. Global mean 30-year trends are shown beneath appropriate map with their uncertainties in brackets. Thus, 5 and 95 percentiles are calculated from subtracting and adding the quantities in brackets to the global mean trends.

uptake by the ocean, the good agreement between model simulation and observations could be due in part to a cancellation of errors—for example, too high a climate sensitivity combined with too low an historical forcing. Hence, our result does not remove the need to reduce uncertainty in these factors, particularly as these might not cancel in the future.

Finally, we apply a comprehensive test for consistency on multiple space- and time-scales by comparing observed and modeled near-surface temperatures for the period 1900–1999 over all spatial scales greater than 5000 km and 10- to 100-year time scales (34). We find that the observations are consistent with the ALL ensemble over all spatio-temporal modes of variability sampled by the control [the probabilities, or *P* values, that remaining model-data differences are due solely to internal variability (35) range from 0.19 when only global mean values are included in the analysis to 0.10 when the maximum 40 spatiotemporal modes, estimated to be adequately sampled by the control, are included (10)]. The NATURAL ensemble can be conclusively rejected on this measure alone [*P* values less than 3×10^{-4} , although 0.03 is the lowest value that can be robustly estimated given the available length of data (35)], and the ANTHRO ensemble appears consistently less likely than the ALL ensemble as an account of observed near-surface temperature changes (*P* values of 0.01 for global mean values and 0.06 if all 40 spatiotemporal modes are included). Our analysis indicates that only the ALL ensemble is consistent with the observations at the *P* = 0.05 confidence level over a wide range of spatial and temporal scales. In addition, a detection and attribution analysis shows that the null-hypothesis of zero amplitude of both natural and anthropogenic signals can be rejected in a two-way regression (10). We conclude therefore, that both anthropogenic and natural factors are required to account for 20th century near-surface temperature change.

The HadCM3 ALL ensemble successfully simulates large-scale temperature changes over the 20th century. However, the model does not capture observed changes in the Atlantic in the early part of the century, nor does it simulate the rise in the North Atlantic Oscillation index observed over the last three decades (36). It may be that the model does not sufficiently resolve the stratosphere (37) or that there are deficiencies in generating or responding to sea surface temperature variations (38). Observational errors are thought to be relatively small (39). If internal variability is underestimated in our model, our consistency tests would then be too stringent and our *P* values would be underestimated; consistency between observations and model at a certain significance level would then be easier to achieve.

There are considerable uncertainties in some of the forcings used in this analysis. The model simulates roughly half the present-day concentrations of sulfate aerosol observed over Europe (40), and will therefore underestimate their direct cooling effect. However, there may be some compensation from omitting the warming effect of black carbon aerosols. The indirect cooling effect may be overestimated, even with too small a sulfate aerosol change, if the simulated natural background aerosol concentrations are also underestimated. In addition, we have not included the indirect cooling effect of sulfate aerosols via cloud lifetime (41). Nevertheless, a regression analysis (10) indicates that the amplitude of the model's response pattern to the combined forcing due to changes in tropospheric ozone and the direct and indirect effects of sulfate aerosols is approximately correct. If there are compensating errors within the sulfate forcing and response, the same cancellation is likely to operate in the future, provided the overall characteristics of sulfate emissions remain unchanged. Cancellation of errors between the sulfate and greenhouse responses is, however, likely to be less effective under the SRES B2 scenario, according to which sulfur emissions are forecast to decrease over the coming decades (42). The solar and volcanic forcings we use are derived from reconstructions based on proxy data and are therefore also subject to considerable uncertainties, although recent explosive volcanic eruptions are likely to have cooled climate, and independent records of solar activity levels inferred from the cosmogenic isotope ¹⁰Be (43) and geomagnetic records (44) provide support to reconstructions (22, 45) that show generally increasing solar activity during the 20th century (12).

Despite these uncertainties, the overall large-scale pattern of observed near-surface temperature change over the 20th century is consistent with our understanding of the combined impacts of natural and anthropogenic forcings. Natural forcings were relatively more important in the early-century warming and anthropogenic forcings have played a dominant role in warming observed in recent decades (10, 13). External forcings appear to be the main contributors controlling near-surface decadal-mean temperature changes on global and continental land scales. Our successful hindcast of large-scale temperature changes over the 20th century increases our confidence in predictions of the anthropogenic contribution to future temperature changes. A prediction for the SRES B2 scenario of future greenhouse gas emissions shows that global mean temperatures continue to increase at a rate similar to that observed over the last three decades.

References and Notes

1. B. D. Santer *et al.*, *Nature* **382**, 39 (1996).
2. G. C. Hegerl *et al.*, *J. Clim.* **9**, 2281 (1996).
3. S. F. B. Tett, P. A. Stott, M. R. Allen, W. J. Ingram, J. F. B. Mitchell, *Nature* **399**, 569 (1999).

4. M. E. Mann, R. S. Bradley, M. K. Hughes, *Geophys. Res. Lett.* **26**, 759 (1999).
5. T. J. Crowley, *Science* **289**, 270 (2000).
6. P. M. Kelly, T. M. L. Wigley, *Nature* **360**, 328 (1992).
7. N. G. Andronova, M. E. Schlesinger, *Geophys. Res. Lett.* **27**, 2137 (2000).
8. J. F. B. Mitchell, T. C. Johns, J. M. Gregory, S. F. B. Tett, *Nature* **376**, 501 (1995).
9. G. C. Hegerl *et al.*, *Clim. Dyn.* **13**, 613 (1997).
10. S. F. B. Tett *et al.*, *Hadley Centre Technical Note No. 19* (Hadley Centre for Climate Prediction and Research, Bracknell, UK, 2000).
11. T. J. Crowley, K.-Y. Kim, *Geophys. Res. Lett.* **26**, 1901 (1999).
12. J. Lean, D. Rind, *J. Clim.* **11**, 3069 (1998).
13. P. A. Stott *et al.*, *Clim. Dyn.* **17**, 1 (2001).
14. T. L. Delworth, T. R. Knutson, *Science* **287**, 2246 (2000).
15. D. Schimel *et al.*, *Climate Change 1995: The Science of Climate Change*, J. T. Houghton *et al.*, Eds. (Cambridge Univ. Press, Cambridge, 1996), chap. 4, pp. 65–131.
16. C. Gordon *et al.*, *Clim. Dyn.* **16**, 147 (2001).
17. V. D. Pope, M. L. Gallani, P. R. Rowntree, R. A. Stratton, *Clim. Dyn.* **16**, 123 (2000).
18. The atmospheric component of HadCM3 has a horizontal grid spacing of 2.5° in latitude by 3.75° in longitude and 19 vertical levels. The oceanic component has 20 vertical levels on a 1.25° by 1.25° grid. Unlike its predecessor, HadCM2, HadCM3 does not require flux adjustments of heat and water at the air-sea interface to maintain a stable climate for multicentury integrations. Model years start on 1 December and annual-mean data from both the model and the observations are calculated from 1 December to 30 November. As a shorthand, dates quoted in the text are given as, for example, 1910 when referring to the year from 1 December 1909 to 30 November 1910.
19. The well-mixed greenhouse gases that are included are CO₂, CH₄, N₂O, and a subset of the halocarbon species considered to be the next largest contributors to anthropogenic forcing, namely CFC₁₁ (CFC-11), CF₂Cl₂ (CFC-12), CF₂ClCFCl₂ (CFC-113), CHF₂Cl (HCFC-22), CF₃CFH₂ (HFC-134a), and C₂H₂F₄ (HFC-125).
20. S. A. Twomey, *Atmos. Environ.* **8**, 1251 (1974).
21. M. Sato, J. E. Hansen, M. P. McCormick, J. B. Pollack, *J. Geophys. Res.* **98**, 22987 (1993).
22. J. Lean, J. Beer, R. Bradley, *Geophys. Res. Lett.* **22**, 3195 (1995).
23. N. Nakicenovic *et al.*, *IPCC Special Report on Emissions Scenarios* (Cambridge Univ. Press, Cambridge, 2000).
24. The SRES B2 scenario results in carbon dioxide emissions from fossil fuels of 9.0, 11.2, and 13.8 Gt C/year, methane emissions of 384, 505, and 597 Mt CH₄/year, and sulfur dioxide emissions of 61, 56, and 48 Mt S/year in 2020, 2050, and 2080, respectively. Further details are given in (23).
25. The patterns of future stratospheric ozone depletion are assumed to be the same as the patterns of present-day ozone depletion, scaled by atmospheric chlorine loading assuming that the Montreal Protocol is followed. From the start of 2000, total solar irradiance is assumed to be the average of the 11-year solar cycle from 1989–1999, and we assume that there are no future explosive volcanic eruptions.
26. The 30-year trends are calculated from 1 December 1969 to 30 November 1999.
27. Uncertainties are calculated by taking 30-year trends from 1110 years of the HadCM3 control, masked by the observations for the 30-year period in question, and calculating the 5 and 95 percentiles of the distribution of these trends. The uncertainty limits are inflated by a factor $\sqrt{1+1/4}$ to take account of uncertainty in the single observation and the four-member model ensemble mean.
28. The ensemble mean trend from the four simulations was compared with the observed trend at each grid point using a local two-sided two-sample *t* test. The variance was estimated from 37 nonoverlapping 30-year trends taken from the control simulation and the number of degrees of freedom was assumed to be 37.
29. M. A. Cane *et al.*, *Science* **275**, 957 (1997).

30. Subdecadal correlations are based on annual mean data after removing a 10-year running mean. The 10- to 50-year correlations are based on the difference between the 10- and 50-year running means, and greater than 10-year correlations are based on 10-year running means alone. The threshold for significance (at the $P = 0.05$ level) for the sub-10-year, 10 to 50-year, and greater than 10-year correlations are 0.15, 0.62, and 0.47, respectively.
31. Potential predictability is given by

$$\frac{\text{var(ens. mean)} - \text{var(control)}/4}{\text{var(ens. mean)} - \text{var(control)}/4 + \text{var(control)}}$$

where var(ens. mean) is the variance of the decadal mean temperatures in the ensemble mean and var(control) is the variance of the decadal mean temperatures in the control integration. The $\text{var(control)}/4$ terms account for finite ensemble size, giving a measure of potential skill in predicting a single observed series with a hypothetical infinite ensemble, assuming (as appears to be the case for all diagnostics considered) linear superposition of signals and noise, and normal distributions.

32. G. J. Boer, *Clim. Dyn.* **16**, 469 (2000).

33. M. Collins, M. R. Allen, *Hadley Centre Technical Note*

No. 27 (Hadley Centre for Climate Prediction and Research, Bracknell, UK, 2000).

34. We apply a standard optimal detection methodology, as used in previous studies (3, 73, 35) by projecting decadal mean temperature changes onto the main modes of internal variability. The procedure is optimal in giving more weight to less variable components of the patterns. We calculate the probability that the ensemble mean is consistent with the observations, where the details of the optimization procedure are given in Tett *et al.* (10) and we do not scale the ALL signal. We analyze the period 1 December 1899 to 30 November 1999 and restrict the analysis to the highest 40 spatiotemporal modes of variability, the maximum that is estimated to be adequately sampled by the control (10).
35. M. R. Allen, S. F. B. Tett, *Clim. Dyn.* **15**, 419 (1999).
36. P. A. Stott, S. F. B. Tett, G. S. Jones, M. R. Allen, J. F. B. Mitchell, G. J. Jenkins, data not shown.
37. D. T. Shindell, R. L. Miller, G. A. Schmidt, L. Pandolfo, *Nature* **399**, 452 (1999).
38. T. J. Osborn, K. R. Briffa, S. F. B. Tett, P. D. Jones, R. M. Trigo, *Clim. Dyn.* **15**, 685 (1999).
39. D. E. Parker, P. D. Jones, C. K. Folland, A. Bevan, *J. Geophys. Res.* **99**, 14373 (1994).
40. A. Jones, D. L. Roberts, M. J. Woodage, *Hadley Centre*

Technical Note No. 14 (Hadley Centre for Climate Prediction and Research, Bracknell, UK, 1999).

41. B. A. Albrecht, *Science* **245**, 1227 (1989).
42. M. R. Allen, P. A. Stott, J. F. B. Mitchell, R. Schnur, T. L. Delworth, *Nature* **407**, 617 (2000).
43. J. U. Beer *et al.*, in *The Sun as a Variable Star: Solar and Stellar Irradiance Variability*, Proceedings of IAU Colloquium 143, 20 to 25 June 1993, J. M. Pap, C. Frohlich, H. S. Hudson, S. K. Solanki, Eds. (Cambridge University Press, Cambridge, 1994), pp. 291–300.
44. M. Lockwood, R. Stamper, M. N. Wild, *Nature* **399**, 437 (1999).
45. D. V. Hoyt, K. H. Schatten, *J. Geophys. Res.* **98**, 18895 (1993).
46. P.A.S., S.F.B.T., G.S.J., and G.J.J. were funded by the UK Department of the Environment, Transport and the Regions under contract PECD 7/12/37. M.R.A. was supported by a Research Fellowship from the UK Natural Environmental Research Council. J.F.B.M. was supported by the UK Public Meteorological Service Research and Development Programme. Supplementary support was provided by European Commission contract ENV4-CT97-0501 (QUARCC). We thank the reviewers and N. Rayner for their comments on the manuscript, and the many colleagues who developed HadCM3.

11 September 2000; accepted 7 November 2000

Extended Life-Span Conferred by Cotransporter Gene Mutations in *Drosophila*

Blanka Rogina, Robert A. Reenan, Steven P. Nilsen, Stephen L. Helfand*

Aging is genetically determined and environmentally modulated. In a study of longevity in the adult fruit fly, *Drosophila melanogaster*, we found that five independent P-element insertional mutations in a single gene resulted in a near doubling of the average adult life-span without a decline in fertility or physical activity. Sequence analysis revealed that the product of this gene, named *Indy* (for *I'm not dead yet*), is most closely related to a mammalian sodium dicarboxylate cotransporter—a membrane protein that transports Krebs cycle intermediates. *Indy* was most abundantly expressed in the fat body, midgut, and oenocytes: the principal sites of intermediary metabolism in the fly. Excision of the P element resulted in a reversion to normal life-span. These mutations may create a metabolic state that mimics caloric restriction, which has been shown to extend life-span.

Single gene mutations can greatly enhance our understanding of complex biological processes such as aging. Mutations in *Caenorhabditis elegans* and mice have highlighted the importance of hormone signal transduction, mitochondrial function, food intake, and the growth hormone–prolactin–thyroid-stimulating hormone system in life-span extension (1–9). To date, only one mutation that extends life-span in *Drosophila* has been reported. A partial loss-of-function mutation in the *methuselah* (*mth*) gene extends the average life-span of *Drosophila* by 35%, but nei-

ther the function of the *methuselah* gene product nor its tissue localization is known (10). In mammals, the only intervention that extends life-span is caloric restriction, and it has been postulated that the mechanism by which some of the mutations in *C. elegans* (for example, *daf*) extend life-span may be through a similar alteration in energy use (5–7).

In studies of *Drosophila* enhancer-trap lines (11), we noticed that male and female flies of two lines, 206 and 302, showed a doubling of mean life-span (from ~37 to ~70 days) and a 50% increase in maximal life-span. This occurred when only one copy of the enhancer-trap chromosome was present (in heterozygotes) (Fig. 1). Chromosomal *in situ* hybridization revealed that the P element in both 206 and 302 was inserted at the same cytological location (12). Genomic

DNA flanking the site of insertion in the two enhancer-trap lines (206 and 302) was obtained by plasmid rescue (13) and sequenced. The insertion sites in the 206 and 302 enhancer-trap lines were 5753 base pairs (bp) from each other and were in the same gene, which we have named *Indy* (for *I'm not dead yet*).

Sequence analysis identified three expressed sequence tags (ESTs) from the *Drosophila* genome project (LD13803, LD16220, and HL01773). Genomic and cDNA sequences predicted a 572–amino acid protein with 34% identity and 50% similarity to human and rat renal sodium dicarboxylate cotransporters (14–16) (Fig. 2). Mammalian dicarboxylate cotransporters are membrane proteins responsible for the uptake or reuptake of di- and tricarboxylic acid Krebs cycle intermediates such as succinate, citrate, and alpha-ketoglutarate. They are found in a variety of tissues, including brush border cells of the small intestine, colon, and placenta; the basolateral membrane of perivascular cells in the liver; and epithelial cells of the renal proximal tubule and the brain (14–16).

Information on the chromosomal location of *Indy* was used to identify additional mutations in the *Indy* gene from other laboratories. We examined several candidate lines with P-element insertions in the same cytogenetic region as *Indy* and found a third enhancer-trap line with a P element inserted 734 bp from the site of the 206 insertion (Fig. 2A). As a heterozygote, this line, 159, showed the same extension in life-span (Fig. 1). Two further P-element insertions in *Indy* were obtained through site-selected mutagenesis of the *Indy* locus. In a polymerase chain reaction–based screen of 10,000 mutagenized third chromosomes, we identified two new insertions into the *Indy* locus (12) (Fig. 2A). Flies heterozygous for either of these new alleles of *Indy* also showed a large extension in life-span (12).

Department of Genetics and Developmental Biology, School of Medicine, University of Connecticut Health Center, 263 Farmington Avenue, Farmington CT 06030, USA.

*To whom correspondence should be addressed. E-mail: shelfand@neuron.uconn.edu